A constitutive framework for rocks undergoing solid dissolution

Ronaldo I. Borja[1,*] · Wei Chen[1] · Alesanmi R. Odufisan[1]

[1]Department of Civil and Environmental Engineering, Stanford University, Stanford, CA 94305, USA. *E-mail: `borja@stanford.edu`

Summary. We formulate a time-dependent damage theory for rocks subjected to mechanical deformation and solid dissolution. The constitutive description is inspired by the transition state theory, which states that the rate of dissolution is a function of the reactive surface area measured through the crack density in the volume. We use a gradient-enhanced damage framework in which damage depends on the deformation of the material as well as on the amount of solid mass dissolved over time. The gradient-enhanced formulation is characterized by a three-field variational formulation with the solid displacement, nonlocal equivalent strain, and nonlocal rate of solid dissolution as the basic state variables. Traditionally, time-independent damage theories have only allowed damage to increase with increasing external load. In the proposed framework, the degree of damage may increase due to solid dissolution even when the external load is held fixed. In this way, solid dissolution is viewed as a process that is responsible for bringing about rate-dependent effects such as creep and stress-relaxation, which are two common features of geomaterial behavior.

Keywords. Chemical damage, damage mechanics, fracture, mechanical damage, solid dissolution

1 Introduction

We present a mathematical framework for damage in solids that accommodates both mechanical deformation and chemical reaction. Solid deformation results in mechanical damage in which the solid body loses a portion of its full capacity to resist a given load. Chemical reaction results in solid dissolution, which occurs in rocks, for example, when fluids such as fresh water and/or supercritical CO_2 are injected into a fracture [35], causing minerals such as salt, calcite, and sodium bicarbonate to dissolve. We note that whereas mechanical damage is mass-conserving, chemical damage causes the solid volume to lose mass, resulting in a porosity increase.

In rocks, dissolution of minerals triggered by CO_2 injection can alter the overall porosity and intrinsic permeability of the material [1, 103]. For a carbonate-rich formation, facilitated dissolution of carbonate minerals enlarges pores, increases porosity, and creates preferential flow paths [36, 40, 58, 85, 86]. CO_2 also dissolves aluminosilicate minerals, and their secondary product can re-precipitate once the brine is over-saturated [31]. In shale, constant exposure to a large amount of CO_2 typically results in damage in the form of degradation of stiffness and strength as revealed in the results of a variety of laboratory tests, including Brazilian split test [34], uniaxial compression tests [37, 65, 66, 92, 94], uniaxial tension tests [3], and triaxial compression test [3].

Apart from the actions of CO_2 and fresh water on rocks, another example of chemical damage is calcium leaching in cementitious materials when exposed to hydrochloric acid solution. In general, chemical damage is dependent on the solvent concentration [52, 57, 92], and could occur once a certain value of the volumetric expansive strain is exceeded [92]. Solid dissolution is also dependent on the reaction area or crack density, so that evolution laws based on the volumetric strain have been traditionally used to capture the mechanical behavior of concrete under coupled axial loading and sulfate attack [60, 76, 91].

Fluids have more difficulty invading the pores of rock or concrete because of the very small size of the pores and low bulk permeability of the matrix [4, 38, 69]. But with open and connected fractures and microcracks, the accessibility of the solid matrix to host fluids is greatly enhanced, promoting dissolution due to increased specific surface area that is exposed to chemical reaction [41, 48]. Thus, it can be expected that solid dissolution is more likely to occur in regions where the fracture density is high than in regions where the fracture density is low [2, 6].

Continuum damage mechanics has long been used in engineering research to model the initiation, propagation, and fracture of materials [73, 74, 79, 82]. The theory has been applied to both brittle materials such concrete [68] as well as to more ductile and weaker materials such as salt rock [81, 90]. Experiments have shown that a zone consisting of numerous microcracks develops when a load is applied on the material [70]. The density of the microcracks increases with increasing load, resulting in a reduced effective area available for resisting the load. Damage theory has now been successfully combined with plasticity [8, 9, 87] and poromechanics [63] to address both isotropic and anisotropic damage [47]. Oftentimes, the principles of thermodynamics have been used to develop combination theories [77]. As for the numerical implementation of the continuum damage theory, an implicit gradient method for damage is especially suited for simulating microcracking in rock or concrete [73], as well as for capturing the heterogeneous distribution of the microcrack density.

In this paper we present a novel framework for damage mechanics in solids experiencing both mechanical and chemical damage. Key features of the formulation include a multiplicative application of damage formula for mechanical and chemical damage and a three-field gradient-enhanced formulation to regularize an ill-posed problem. Inspired by the transition state theory for chemical damage, microcracks are assumed to open when the dilatational strain reaches a certain threshold value, with the rate of solid dissolution saturating to an asymptotic value at infinite dilatational strain. Conservation laws for mass and momentum are written to include the rate of loss of mass, which is factored into the finite element formulation. Traditionally, damage theories have only allowed damage to increase with increasing external load. A novelty of the proposed framework is that localized damage can now increase even with a fixed external load due to solid dissolution. This allows rate-dependent effects induced by solid dissolution, such as creep and stress relaxation, to be simulated without using any rate-dependent constitutive theory [13, 24, 93].

The order of presentation is as follows. Section 2 formulates the combined mechanical and chemical damage problem. Section 3 introduces a three-field set of gradient-enhanced variational equations for subsequent finite element implementation. Section 4 presents some results of numerical simulations including the dissolution of clay minerals in a heterogeneous shale rock. As for notations, scalar quantities are denoted in lightfaced symbols; vectors, tensors, and matrices are written in boldfaced notation.

2 Theory

This section presents the mathematical formulation of the combined theory of mechanical and chemical damage. All throughout the presentation, the material is assumed to be isotropic and the deformation is infinitesimal.

2.1 Conservation laws

We recall the mass and momentum balance for a solid that is losing mass at the rate of $\dot{m} < 0$ per unit total volume of the solid in the current configuration. The law of conservation of mass in Eulerian form is given by

$$\frac{\mathrm{d}\rho}{\mathrm{d}t} + \rho \operatorname{div} \boldsymbol{v} = \dot{m} \,, \tag{1}$$

where $\mathrm{d}(\cdot)/\mathrm{d}t$ is the material time derivative following the motion of the solid, ρ is the overall mass density of the solid in the current configuration (mass of solid divided by total volume in current configuration), and $\boldsymbol{v}$ is the solid velocity. For a rock containing soluble minerals $\alpha = 1, 2, \ldots, N$, the rate of dissolution per unit total volume of the rock is given by

$$\dot{m} = \sum_{\alpha=1}^{N} \dot{\mu}_{\alpha} \phi^{\alpha} \,, \tag{2}$$

where $\dot{\mu}_\alpha$ is the rate of dissolution of mineral α per unit current volume of the same mineral, and $\phi^\alpha = \mathrm{d}V^\alpha/\mathrm{d}V$ is the volume fraction of the rock mineral. In Lagrangian form, the mass balance equation is given by

$$\frac{\mathrm{d}\rho_0}{\mathrm{d}t} = \dot{m}_0\,, \tag{3}$$

where $\rho_0 = \rho J$, J is the Jacobian of the motion, and $\dot{m}_0$ is the pull-back rate of dissolution, which is given by

$$\dot{m}_0 = \dot{m}J = \sum_{\alpha=1}^{N} \dot{\mu}_\alpha \phi_0^\alpha\,, \tag{4}$$

with $\phi_0^\alpha = J\phi^\alpha = \mathrm{d}V^\alpha/\mathrm{d}V_0$ being the pull-back volume fraction of mineral α. Note that $\mathrm{d}\rho_0/\mathrm{d}t = 0$ if the solid mass is conserved.

The term $\dot{m}$ carries over to the momentum balance equation in the following manner. In Eulerian form, the linear momentum balance is given by [15]

$$\nabla \cdot \boldsymbol{\sigma} + \rho \boldsymbol{g} = \dot{m}\boldsymbol{v} + \rho \boldsymbol{a}\,, \tag{5}$$

where $\boldsymbol{\sigma}$ is the Cauchy stress tensor, $\nabla \cdot (\,)$ is the Eulerian divergence operator, $\boldsymbol{g}$ is the gravity acceleration vector, and $\boldsymbol{a}$ is the material acceleration. In Lagrangian form, the balance of linear momentum is given by

$$\nabla_X \cdot \boldsymbol{P} + \rho_0 \boldsymbol{g} = \dot{m}_0 \boldsymbol{v} + \rho_0 \boldsymbol{a}\,, \tag{6}$$

where $\boldsymbol{P}$ is the first Piola-Kirchhoff stress tensor and $\nabla_X \cdot (\,)$ is the Lagrangian divergence operator. For quasi-static loading, $\boldsymbol{a} = \boldsymbol{0}$.

2.2 Combined mechanical and chemical damage

A typical rock sample consists of minerals and organic materials with varying degrees of solubility. Calcite, for example, is soluble when exposed to CO_2, but quartz is relatively insoluble. However, for calcite to dissolve it must be exposed to a reactive fluid such as CO_2. This is facilitated by mechanical damage in the form of microcracks. The more microcracks there are in the rock, the more calcites the fluid will dissolve. Thus, two types of damage may arise: chemical damage leading to porosity increase, and mechanical damage due to solid deformation. Herein we consider an elastic-damage constitutive law of the form

$$\boldsymbol{\sigma} = (1 - D_m)(1 - D_c)\mathbb{C}^e : \boldsymbol{\epsilon}\,, \tag{7}$$

where $\mathbb{C}^e$ is a rank-four tensor of elastic moduli, $\boldsymbol{\epsilon}$ is the infinitesimal strain tensor, D_m is a mechanical damage variable induced by the solid deformation, and D_c is a chemical damage variable induced by the solid dissolution.

The rationale behind the above constitutive framework is that $\boldsymbol{\sigma}' = \boldsymbol{\sigma}/(1 - D_c)$ would be the intrinsic Cauchy stress of the undeformed solid in the presence of the void spaces created by the dissolved solid. Therefore, $\boldsymbol{\sigma}'' = \boldsymbol{\sigma}'/(1-D_m) \equiv \mathbb{C}^e : \boldsymbol{\epsilon}$ must be the intrinsic stress in the deformed solid in the presence of the void spaces created by the dissolved solid. Both D_m and D_c in Equation (7) can range from zero to one, although D_c may be limited to a smaller number depending on the amount of soluble minerals in the rock.

Expanding Equation (7) yields

$$\boldsymbol{\sigma} = (1-D)\mathbb{C}^e : \boldsymbol{\epsilon}\,, \tag{8}$$

where

$$D = D_m + D_c - D_m D_c\,. \tag{9}$$

If both D_m and D_c are small, their product term may be ignored and the linearized damage variable takes the form

$$D = D_m + D_c\,. \tag{10}$$

Because we shall consider the entire range of values of the damage variable, we consider the fully nonlinear damage Equation (9).

2.3 Mechanical damage

For mechanical damage, we consider the standard framework described in [51, 73] in which the damage variable D_m varies with some internal strain history variable κ according to the equation first proposed by Mazars and Pijaudier-Cabot [68] of the form

$$D_m(\kappa) = 1 - \frac{\kappa_0}{\kappa}\left((1-a) + a e^{-b\Delta\kappa}\right)\,, \tag{11}$$

where $\Delta\kappa = \kappa - \kappa_0 \geq 0$, κ_0 is an initial threshold value of κ above which damage starts to occur, and a and b are material parameters. The monotonically increasing κ defines the maximum value attained by a nonlocal equivalent strain measure $\bar{\varepsilon}_{\text{eq}}$, whose local value ε_{eq} is taken to be of the form proposed by de Vree et al. [26] as

$$\varepsilon_{\text{eq}} = \frac{k-1}{2k(1-2\nu)} I_1 + \frac{1}{2k}\sqrt{\frac{(k-1)^2}{(1-2\nu)^2} I_1^2 + \frac{2k}{(1+\nu)^2} J_2}\,, \tag{12}$$

where $I_1 = \text{tr}(\boldsymbol{\epsilon})$ and $J_2 = 3\text{tr}(\boldsymbol{\epsilon}\cdot\boldsymbol{\epsilon}) - \text{tr}^2(\boldsymbol{\epsilon})$ are the invariants of the strain tensor $\boldsymbol{\epsilon}$, ν is the Poisson's ratio, and k is a parameter that accounts for non-identical responses of the material in tension and compression. The nonlocal equivalent strain is then evaluated according to the equation [75]

$$\bar{\varepsilon}_{\text{eq}} = \frac{1}{\mathcal{B}} \int_{\mathcal{B}} g(\boldsymbol{\xi}) \varepsilon_{\text{eq}}(\boldsymbol{x}+\boldsymbol{\xi})\,\text{d}V\,, \quad \frac{1}{\mathcal{B}}\int_{\mathcal{B}} g(\boldsymbol{\xi})\,\text{d}V = 1\,, \tag{13}$$

where $g(\boldsymbol{\xi})$ is a weight function similar to the kernels used in SPH [27, 28, 32, 33] and $\mathcal{B}$ is the domain of nonlocality (could be the entire domain, see [72]).

The strain variables $\bar{\varepsilon}_{\text{eq}}$ and κ are related by the Karush-Kuhn-Tucker conditions [14]

$$\dot{\kappa} \geq 0\,, \quad \bar{\varepsilon}_{\text{eq}} - \kappa \leq 0\,, \quad \dot{\kappa}(\bar{\varepsilon}_{\text{eq}} - \kappa) = 0\,. \tag{14}$$

Using the Taylor series expansion for ε_{eq} about point $\boldsymbol{x}$ and re-arranging yields the following gradient-enhanced form for the equivalent strain [73]

$$\bar{\varepsilon}_{\text{eq}} - \ell_1^2\, \nabla^2 \bar{\varepsilon}_{\text{eq}} = \varepsilon_{\text{eq}}\,, \tag{15}$$

where ∇^2 is the Laplacian operator and ℓ_1 is a length scale parameter.

2.4 Chemical damage

For chemical damage, the rate of change of D_c may be linked directly to the rate of change of solid mass $\dot{m}$ through the equation

$$\dot{D}_c = -\frac{\dot{m}}{\rho_s} = -\frac{\dot{\mu}_s}{\rho_s}\phi^s\,, \tag{16}$$

where ρ_s is the intrinsic mass density of the solid (mass of solid divided by volume of the solid), which should not be confused with the overall mass density ρ (mass of solid divided by the total volume of the material, including the pore spaces), and $\dot{\mu}_s < 0$ is the rate of dissolution of the solid per unit volume of the solid. The underlying assumption here is that the area fraction and volume fraction are statistically equivalent from the point of view of a representative elementary volume. For a rock with soluble minerals $\alpha = 1, \ldots, N$,

$$\dot{D}_c = -\sum_{\alpha=1}^{N} \frac{\dot{\mu}_\alpha}{\rho_\alpha}\phi^\alpha\,, \tag{17}$$

where $\dot{\mu}_\alpha$, ρ_α, and ϕ^α are the rate of dissolution, intrinsic mass density, and volume fraction of mineral α, respectively.

Integrating Equation (16) yields

$$D_c = -\int_t \frac{\dot{\mu}_s}{\rho_s}\phi^s \mathrm{d}t\,. \tag{18}$$

On the other hand, integrating Equation (17) for a heterogeneous rock with soluble minerals $\alpha = 1, \ldots, N$ yields

$$D_c = -\sum_{\alpha=1}^{N} \int_t \frac{\dot{\mu}_\alpha}{\rho_\alpha}\phi^\alpha\, \mathrm{d}t\,. \tag{19}$$

The above expressions for D_c represent the cumulative pore spaces per unit volume created by the dissolved minerals. Theoretically, D_c can range from zero to one, but it could also be a small number depending on the amount of soluble mineral in the rock and/or the amount of reactive species in the fluid.

Solid dissolution is enhanced when the erosive fluid invades the pore spaces through the microcracks within the solid matrix. In rocks, the rate of dissolution of mineral α is often modeled with the transition state theory [55, 56, 71], which states that

$$\dot{\mu}_\alpha = A_\alpha k_0 e^{-E_A/RT} \prod_i a_i^{n_i} f(\Delta G) \,, \tag{20}$$

where A_α is the reactive surface area of mineral α, k_0 is a kinetic reaction rate constant, E_A is the apparent activation energy, R is the universal gas constant, T is temperature, $a_i^{n_i}$ is the activity of aqueous species raised to the exponent n_i, and $f(\Delta G)$ is a function of the thermodynamic potential or driving force. The variable related to mechanical deformation is the reactive surface area A_α of mineral α, which is linked to the microcrack density γ_c in that the higher the microcrack density, the larger the reactive surface area.

Spyropoulos et al. [83] conducted extension experiments on clay and showed that the crack density γ_c increases with the dilative volumetric strain ε_v in a manner shown in Figure 1. The relationship in Figure 1 can be represented by a three-parameter exponential function of the form

$$\gamma_c = C - (C - B) e^{-A\varepsilon_v} \,, \tag{21}$$

where B, C, and $A > 0$ are fitting parameters. This equation predicts that the crack density is equal to B when $\varepsilon_v = 0$ and is equal to C when $\varepsilon_v \to \infty$. Assuming the reactive surface area A_α is proportional to the crack density γ_c, one can construct a similar exponential function for A_α with the same shape as the crack density function γ_c and insert it into Equation (20) to obtain an expression for the rate of mineral dissolution as an exponential function of ε_v.

We now assume that $\dot{\mu}_s$ varies exponentially with ε_v through the three-parameter exponential function

$$\dot{\mu}_s = \dot{\mu}_f - (\dot{\mu}_f - \dot{\mu}_i) e^{-A\varepsilon_v} \,, \tag{22}$$

where $\dot{\mu}_f < 0$, $\dot{\mu}_i < 0$, and $A > 0$ are fitting parameters. Equation (22) predicts a rate of change of solid mass equal to $\dot{\mu}_i$ when $\varepsilon_v = 0$ and $\dot{\mu}_f$ when $\varepsilon_v \to \infty$. Equivalently, we can make the substitution

$$\dot{\mu}_f - \dot{\mu}_i = \dot{\mu}_f e^{A\varepsilon_0} \,, \tag{23}$$

in which case, Equation (22) becomes

$$\dot{\mu}_s = \dot{\mu}_f \left[1 - e^{-A(\varepsilon_v - \varepsilon_0)} \right] . \tag{24}$$

In this new equation, ε_0 takes the role of the third parameter replacing $\dot{\mu}_i$.

The choice between Equations (22) and (24) for the dissolution law depends on the nature of the exponential function. Equation (22) assumes that there is an initial crack density at the volumetrically undeformed state that

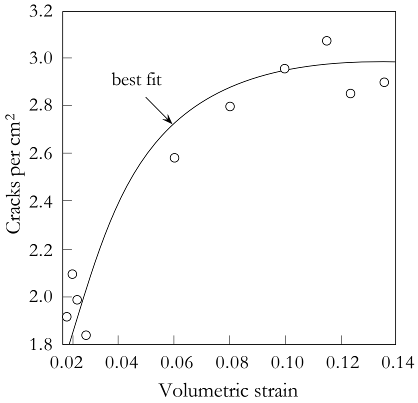

Fig. 1. Variation of crack density with dilative volumetric strain from extension experiments conducted on clay. Best-fit curve gives $\varepsilon_0 \approx -1 \times 10^{-6}$ and $A = 40$. After Spyropoulos et al. [83].

allows the erosive fluid to invade the pore spaces and dissolve the solid. On the other hand, Equation (24) assumes that the solid can only dissolve when the dilative volumetric strain exceeds a critical value ε_0. Note from Equation (23) that

$$\varepsilon_0 = \frac{1}{A} \ln \left(1 - \frac{\dot{\mu}_i}{\dot{\mu}_f} \right) < 0 \,, \tag{25}$$

which means that ε_0 must be compressive if we use the dissolution law of the form given by Equation (22). Because Equation (24) imposes no restriction on the sign of ε_0 while capturing the same exponential variation, we shall adopt this dissolution law in subsequent formulation.

We now consider the condition $\varepsilon_v > \varepsilon_0$ and denote the volumetric overstrain as $\Delta\varepsilon_v = \varepsilon_v - \varepsilon_0 > 0$. Expanding the dissolution law (24) using the Taylor series yields

$$\dot{\mu}_s = \dot{\mu}_f \left[1 - e^{-A\Delta\varepsilon_v} \right] = \dot{\mu}_f \left[A\Delta\varepsilon_v - \frac{1}{2!}(A\Delta\varepsilon_v)^2 + \dots \right] . \tag{26}$$

If $\Delta\varepsilon_v$ is small, the second-order terms may be ignored, and one arrives at the linear equation

$$\dot{\mu}_s \approx A\dot{\mu}_f(\varepsilon_v - \varepsilon_0) = f\varepsilon_v + g \,, \tag{27}$$

where $f = A\dot{\mu}_f$ and $g = -f\varepsilon_0$. This equation agrees with the linear constitutive law for solid dissolution proposed by Hueckel and Hu [44].

Extending the formulation to the nonlocal regime, we now let

$$\dot{\mu}_s(\boldsymbol{x}) = \dot{\mu}_f \lambda(\boldsymbol{x}) \,, \qquad \lambda(\boldsymbol{x}) = 1 - e^{-A\Delta\varepsilon_v(\boldsymbol{x})} \,. \tag{28}$$

The nonlocal counterpart of $\dot{\mu}_s$ is obtained by writing $\lambda(\boldsymbol{x})$ as

$$\bar{\lambda}(\boldsymbol{x}) = \frac{1}{\mathcal{B}'} \int_{\mathcal{B}'} g(\boldsymbol{\xi}) \lambda(\boldsymbol{x} + \boldsymbol{\xi}) \, \mathrm{d}V \tag{29}$$

and taking the nonlocal version as

$$\dot{\bar{\mu}}_s(\boldsymbol{x}) = \dot{\mu}_f \bar{\lambda}(\boldsymbol{x}) \,, \tag{30}$$

where $\mathcal{B}'$ is the domain of nonlocality, herein taken as the entire domain $\mathcal{B}$. This yields the nonlocal rate of dissolution $\dot{\bar{m}}$ given by

$$\dot{\bar{m}} = \dot{\mu}_f \phi^s \bar{\lambda}(\boldsymbol{x}) \,. \tag{31}$$

If a rock contains multiple soluble minerals $\alpha = 1, \ldots, N$, then

$$\dot{\bar{m}}(\boldsymbol{x}) = \Big(\sum_{\alpha=1}^{N} \dot{\mu}_{\alpha f} \phi^{\alpha} \Big) \bar{\lambda}(\boldsymbol{x}) \,, \tag{32}$$

where $\dot{\mu}_{\alpha f}$ is the maximum rate of dissolution of mineral α per unit volume of the same mineral. Regardless of whether the rock contains one or multiple soluble minerals, we see that the nonlocality is factored out of the individual mineral properties through the term $\bar{\lambda}(\boldsymbol{x})$.

Using the Taylor series expansion for λ once again, a gradient-enhanced form is obtained as

$$\bar{\lambda} - \ell_2^2 \, \nabla^2 \bar{\lambda} = \lambda \,, \tag{33}$$

where ℓ_2 is another length scale parameter. The nonlocal rate $\dot{\bar{m}}$ may then be used in lieu of $\dot{m}$ in equation (16). In this case, the damage variable D_c at time $t \in [t_n, t_{n+}]$, assuming the intrinsic solid mass density ρ_s remains constant, now takes the form (for $\alpha = s$)

$$D_c(t) = D_{c,n} + \frac{|\dot{\mu}_f| \bar{\lambda}}{\rho_s} \int_{t_n}^{t} \phi^s \, \mathrm{d}t \,, \tag{34}$$

where $D_{c,n}$ is the value of D_c at time t_n and $\bar{\lambda}$ is the nonlocal value of λ in the time interval $[t_n, t_{n+1}]$. The time-evolution D_c then requires the time-evolution of ϕ^s.

We note that $\dot{D}_c = \dot{\phi}^s$ for a rock with one soluble solid. Thus, using the nonlocal version of $\dot{\mu}_s$ in Equation (16), we obtain

$$\dot{\phi}^s = \frac{\dot{\bar{\mu}}_s}{\rho_s} \phi^s \,. \tag{35}$$

Integrating over the time interval $t \in [t_n, t_{n+1}]$ and assuming that $|\dot{\mu}_f|$ remains constant within this interval yields

$$\phi^s(t) = \phi^s_n \exp \Big[- \frac{|\dot{\mu}_f|}{\rho_s} \bar{\lambda} \big(t - t_n \big) \Big] \,. \tag{36}$$

Substituting this expression into Equation (34) and integrating analytically yields

$$D_c(t) = D_{c,n} + \big(\phi_n^s - \phi^s(t)\big)\,. \tag{37}$$

This equation states that the increase in chemical damage D_c is equal to the reduction in the volume fraction ϕ^s.

A similar evolution may be written for a rock with multiple soluble minerals as follows:

$$\phi^\alpha(t) = \phi_n^\alpha \exp\Big[- \frac{|\dot{\mu}_{\alpha f}|}{\rho_\alpha} \bar{\lambda}\big(t - t_n\big)\Big]\,, \tag{38}$$

for $\alpha = 1, \ldots, N$, assuming the $|\dot{\mu}_{\alpha f}|$'s are constant within the time interval. Integrating Equation (19) incrementally yields

$$D_c(t) = D_{c,n} + \sum_{\alpha=1}^{N} \big(\phi_n^\alpha - \phi^\alpha(t)\big)\,. \tag{39}$$

In this case, the increase in chemical damage is equal to the sum of the reductions in the volume fractions of all soluble minerals in the rock.

2.5 Implications for the stress-strain responses

Because the damage parameter $D_c(t)$ depends on time, the classic elastic-damage formulation is now endowed with rate-dependent effects. We illustrate this feature with the following simple stress-point simulation.

We consider a rock sample under triaxial loading with σ_a as the axial stress and σ_r as the radial stress. We assume that this sample is subjected to isochoric deformation with $\epsilon_r = -\epsilon_a/2$, where ϵ_r and ϵ_a are the radial and axial strains, respectively. The stress-strain relation reduces to the scalar equation

$$\sigma_a - \sigma_r = 3\mu^e(1 - D)\epsilon_a\,, \tag{40}$$

where μ^e is the un-degraded elastic shear modulus and $D = (1 - D_c(t))(1 - D_m)$ is the time-dependent damage parameter.

According to Equation (12), the equivalent strain $\varepsilon_{\rm eq}$ is a function of J_2 alone, and takes the simple form

$$\varepsilon_{\rm eq} = \frac{3}{2\sqrt{k}(1+\nu)}\epsilon_a\,. \tag{41}$$

When $\varepsilon_{\rm eq} \geq \kappa_0$, the mechanical damage in Equation (11) reduces to the form

$$D_m(\varepsilon_{\rm eq}) = 1 - \frac{\kappa_0}{\varepsilon_{\rm eq}}\Big[(1-a) + ae^{-b(\varepsilon_{\rm eq} - \kappa_o)}\Big]\,, \tag{42}$$

which means that D_m is also a nonlinear function of ϵ_a. On the other hand, the chemical damage parameter $D_c(t)$ is given by Equation (37) for a rock

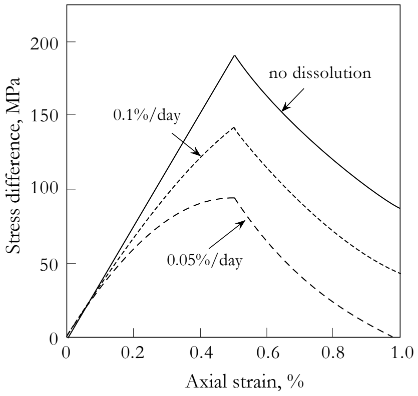

Fig. 2. Triaxial stress-strain curves at different axial strain rates for a rock sample subjected to isochoric deformation. Solid dissolution leads to rate-dependent stress-strain responses. Stress difference $= \sigma_a - \sigma_r$.

with one soluble solid, and by Equation (39) for a rock with multiple soluble solids. But $\varepsilon_v = 0$ from the assumption of isochoric deformation. Therefore, Equation (22) yields $\dot{\mu}_s = \dot{\mu}_i =$ constant, and D_c becomes an exponential function of t. In short, the damage parameter D becomes a nonlinear function of both ϵ_a and t, i.e., $D = D(\epsilon_a, t)$.

Figure 2 shows the stress-strain plots generated from the stress-point simulations assuming the following material parameters: $\mu^e = 12,500$ N/mm^2, $\nu = 0.2$, $k = 10$, $a = 1$, $b = 400$, $\rho_s = 2.4 \times 10^{-6}$ kg/mm^3, $\phi_0^s = 0.8$, and $|\dot{\mu}_i| = 1.5 \times 10^{-7}$ kg/mm^3/day. The simulation assumes that there is already a network of connected micro-fractures that allows the fluid to dissolve the solid at time $t = 0$. The axial strain ϵ_a is then prescribed at different rates allowing solid dissolution while the sample is being deformed. The limiting condition of $\dot{\epsilon}_a \to \infty$ corresponds to instantaneous deformation that does not leave time for the solid to dissolve. As expected, the sample gains strength with increasing strain rate. Note that with a finite strain rate, the elastic modulus degrades even before the stress-strain curve reaches its peak.

2.6 Summary of material parameters

Apart from the elastic constants E and ν, the material parameters required by the mechanical component of the model include the threshold value κ_0 signaling the initiation of mechanical damage, constants a and b defining the exponential decay of strength in the softening range, and the parameter k that differentiates between the tensile and compressive strength of the material.

The parameters of the proposed solid-dissolution model include ε_0, A, and the rates of mineral dissolution $\dot{\mu}_{\alpha f}$ for $\alpha = 1, \ldots, N$. The first two parameters are related to mechanical deformation and may be inferred from the curve generated from extension experiments such as the one shown in Figure 1. The value of ε_0 may be inferred from the ε_v-intercept of the crack density-dilative volumetric strain curve. The value of A may be inferred from the shape of the same experimental curve fitted with an exponential function, and may depend on the ductility or brittleness of the rock: the more brittle the rock, the larger the value of A.

The value of $|\dot{\mu}_{\alpha f}|$ depends on the properties of the mineral and the erosive fluid, as well as on temperature, pH, and other environmental factors [12]. As a general rule, this parameter increases with increasing temperature and/or decreasing pH. Because numerous factors enter into the transition state theory, significant uncertainties exist in calculating the absolute reaction rate constants [84]. Given that the focus of the paper is to establish a link between solid dissolution and mechanical deformation, we shall assume that the temperature, pH, and other environmental factors are fixed for now and take the value of $|\dot{\mu}_{\alpha f}|$ as constant for the specific soluble material of interest.

3 Finite element formulation

The finite element formulation for the boundary-value problem relies on a three-field $\boldsymbol{u}/\bar{\varepsilon}_{\rm eq}/\bar{\lambda}$ variational formulation. The strong form (S) can be stated as follows. Let $\mathcal{B}$ define the domain of the problem and let $\partial\mathcal{B}_u$ and $\partial\mathcal{B}_t$ denote the Dirichlet and Neumann boundaries, respectively. Ignoring the inertia load, we want to find $\boldsymbol{u}$, $\bar{\varepsilon}_{\rm eq}$, and $\bar{\lambda}$ such that

$$\left.\begin{aligned} \nabla \cdot \boldsymbol{\sigma} + \rho \boldsymbol{g} &= \dot{m}\boldsymbol{v} \\ \bar{\varepsilon}_{\rm eq} - \ell_1^2\, \nabla^2 \bar{\varepsilon}_{\rm eq} &= \varepsilon_{\rm eq} \\ \bar{\lambda} - \ell_2^2\, \nabla^2 \bar{\lambda} &= \lambda \end{aligned}\right\} \quad \text{in } \mathcal{B}\,, \tag{43}$$

where $\boldsymbol{v} = \dot{\boldsymbol{u}}$ is the solid velocity. The boundary conditions are

$$\left.\begin{array}{lll} \boldsymbol{u} = \tilde{\boldsymbol{u}} & \text{on} & \partial\mathcal{B}_u \\ \boldsymbol{n} \cdot \boldsymbol{\sigma} = \boldsymbol{t} & \text{on} & \partial\mathcal{B}_t \\ \nabla \bar{\varepsilon}_{\rm eq} \cdot \boldsymbol{n} = 0 & \text{on} & \partial\mathcal{B} \\ \nabla \bar{\lambda} \cdot \boldsymbol{n} = 0 & \text{on} & \partial\mathcal{B} \end{array}\right\}\,, \tag{44}$$

where $\tilde{\boldsymbol{u}}$ and $\boldsymbol{t}$ are the prescribed displacement and traction vectors, respectively. For very slow processes (such as stress relaxation and creep processes), the momentum term $\dot{m}\boldsymbol{v}$ in the equilibrium equation may be ignored.

The weak form (W) of the boundary-value problem can be stated as follows. Let $\mathcal{S} = \{\boldsymbol{u}\,|\,\boldsymbol{u} \in H^1, \boldsymbol{u} = \tilde{\boldsymbol{u}} \text{ on } \partial\mathcal{B}_u\}$ denote the set of trial functions for $\boldsymbol{u}$ and $\mathcal{V} = \{\boldsymbol{\eta} \,|\, \boldsymbol{\eta} \in H^1, \boldsymbol{\eta} = \boldsymbol{0} \text{ on } \partial\mathcal{B}_u\}$ the corresponding set of weighting functions. Further, let $\mathcal{C}^0$ denote the set of continuous functions. We want to find $\boldsymbol{u} \in \mathcal{S}$, $\bar{\varepsilon}_{\text{eq}} \in \mathcal{C}^0$, and $\bar{\lambda} \in \mathcal{C}^0$ such that for all $\boldsymbol{\eta} \in \mathcal{V}$, $\phi \in \mathcal{C}^0$ and $\varphi \in \mathcal{C}^0$, the following variational equations are satisfied:

Equilibrium:

$$\int_{\mathcal{B}} \nabla^s \boldsymbol{\eta} : \boldsymbol{\sigma} \, \mathrm{d}V + \int_{\mathcal{B}} \boldsymbol{\eta} \cdot \dot{m}\boldsymbol{v} \, \mathrm{d}V = \int_{\mathcal{B}} \boldsymbol{\eta} \cdot \rho \boldsymbol{g} \, \mathrm{d}V + \int_{\partial\mathcal{B}} \boldsymbol{\eta} \cdot \boldsymbol{t} \, \mathrm{d}A \, ; \tag{45}$$

Mechanical damage:

$$\int_{\mathcal{B}} (\phi \bar{\varepsilon}_{\text{eq}} + \ell_1^2 \, \nabla\phi \cdot \nabla\bar{\varepsilon}_{\text{eq}}) \, \mathrm{d}V = \int_{\mathcal{B}} \phi \varepsilon_{\text{eq}} \, \mathrm{d}V \, ; \tag{46}$$

Chemical damage:

$$\int_{\mathcal{B}} (\varphi \bar{\lambda} + \ell_2^2 \, \nabla\varphi \cdot \nabla\bar{\lambda}) \, \mathrm{d}V = \int_{\mathcal{B}} \varphi \lambda \, \mathrm{d}V \, . \tag{47}$$

Note that the mass dissolution term is written on the left-hand side of the equilibrium equation since the solid velocity field is unknown.

Mixed finite elements similar to those used in multiphysics problems may be used for the present problem. For the equilibrium condition, the finite element equation in residual form may be written as

$$\boldsymbol{\mathcal{R}}_1 = \int_{\Omega} \boldsymbol{B}^{\mathsf{T}} \hat{\boldsymbol{\sigma}} \, \mathrm{d}V + \int_{\Omega} \boldsymbol{N}^{\mathsf{T}} \dot{m}\boldsymbol{v} \, \mathrm{d}V - \int_{\Omega} \boldsymbol{N}^{\mathsf{T}} \rho \boldsymbol{g} \, \mathrm{d}V - \int_{\partial\Omega} \boldsymbol{N}^{\mathsf{T}} \boldsymbol{t} \, \mathrm{d}A \, , \tag{48}$$

where $\boldsymbol{N}$ is the shape function matrix for the displacement field, $\boldsymbol{B}$ is the strain-displacement transformation matrix, and $\hat{\boldsymbol{\sigma}}$ is the Cauchy stress vector in Voigt form, an implicit function of the solid displacement vector $\boldsymbol{d}$ as well as the damage variables D_m and D_c.

For the gradient enhancements, we select the same interpolation functions for ϕ, φ, $\bar{\varepsilon}_{\text{eq}}$, and $\bar{\lambda}$, herein represented by the shape function matrix $\tilde{\boldsymbol{N}}$ with gradient $\boldsymbol{E} = \nabla\tilde{\boldsymbol{N}}$. The mechanical damage enhancement in residual form is given by

$$\boldsymbol{\mathcal{R}}_2 = \Big(\int_{\Omega} \tilde{\boldsymbol{N}}^{\mathsf{T}} \tilde{\boldsymbol{N}} \, \mathrm{d}V + \int_{\Omega} \boldsymbol{E}^{\mathsf{T}} \ell_1^2 \, \boldsymbol{E} \, \mathrm{d}V \Big) \boldsymbol{e} - \int_{\Omega} \tilde{\boldsymbol{N}}^{\mathsf{T}} \varepsilon_{\text{eq}} \, \mathrm{d}V \, , \tag{49}$$

where $\boldsymbol{e}$ is the vector of nodal values of $\bar{\varepsilon}_{\text{eq}}$. The chemical damage enhancement takes a similar form:

$$\boldsymbol{\mathcal{R}}_3 = \Big(\int_{\Omega} \tilde{\boldsymbol{N}}^{\mathsf{T}} \tilde{\boldsymbol{N}} \, \mathrm{d}V + \int_{\Omega} \boldsymbol{E}^{\mathsf{T}} \ell_2^2 \, \boldsymbol{E} \, \mathrm{d}V \Big) \boldsymbol{l} - \int_{\Omega} \tilde{\boldsymbol{N}}^{\mathsf{T}} \lambda \, \mathrm{d}V \, , \tag{50}$$

where $\boldsymbol{l}$ is the vector of nodal values of $\bar{\lambda}$. The solutions $\boldsymbol{d}^*$, $\boldsymbol{e}^*$, and $\boldsymbol{l}^*$ satisfy the conditions $\boldsymbol{\mathcal{R}}_i = \boldsymbol{0}$ for $i = 1, 2, 3$, and are obtained iteratively via Newton's method (see Appendix A).

4 Numerical examples

For the numerical examples presented in this section, the effects of gravity were ignored. The focus of the studies was on the impact of dissolution damage on the mechanical behavior of the rock. The first example validates the constitutive model against the experimental data on creep of a limestone induced by solid dissolution. The next three examples present boundary-value problems that investigate the sensitivity of the finite element solutions to mesh refinement and to variations in material properties. The fifth example utilizes the reported solubility properties of kaolinite taken from the literature and investigates the combined effects of mechanical and chemical damage around a crack tip in a clay rock due to the injection of an erosive fluid.

For the simulation of boundary-value problems, both creep and relaxation tests were conducted on structures of different configurations. Equal-order interpolations of the type Q1P1P1, similar to those used in poromechanics but with no stabilization [16, 22, 23, 95, 96, 99], were used for these problems. No oscillations were observed in all the examples despite the lack of stabilization [19, 20, 89, 98], which could be attributed to the fact that none of the diagonal block matrices in the tangent operator is zero (see Appendix A).

4.1 Dissolution of a limestone

There have been a few chemo-mechanical laboratory studies conducted on carbonate rocks reported in the literature [58, 67]. In this section, we validate the chemical damage model using the creep experiment conducted by Le Guen et al. [58] on Lavoux W520 limestone subjected to CO_2 exposure.

The experiment consisted of a cylindrical sample of limestone having a diameter of 23 mm and a height of 48 mm. The creep response of this sample is shown in Figure 3. The sample was first stabilized under a fixed axial stress of $\sigma_a = -16.3$ MPa and a fixed radial stress of $\sigma_r = -11.6$ MPa (both compressive) in the absence of fluid. During this time, no noticeable axial creep strain was observed in the sample (see the nearly horizontal line up to time of around 44 days in Figure 3). Afterwards, CO_2 saline solution was injected into the sample at a pressure of $p_f = 7.9$ MPa to induce solid dissolution on the rock. Continuous supply of fluid was maintained to ensure that reactive agents were available throughout the duration of the experiment .

To obtain the mechanical deformation response, the Terzaghi effective stress equation was employed in the simulation, which is given by the equations

$$\sigma'_a = \sigma_a + p_f \,, \qquad \sigma'_r = \sigma_r + p_f \,, \tag{51}$$

where the continuum mechanics convention for the normal stresses was employed. Strictly speaking, one must introduce the Biot coefficient into the above equations [17], but nevertheless, we employed the Terzaghi effective stress equation since this is what the authors used in their paper [58]. This results in an axial effective stress of $\sigma'_a = -8.8$ MPa and a radial effective stress of $\sigma_r = -3.7$ MPa.

For a given Young's modulus E and Poisson's ratio ν, Hooke's law with damage reads

$$\left.\begin{aligned}(1-D)\epsilon_a &= \frac{1}{E}\big[\sigma_a - \nu(\sigma_r + \sigma_r)\big]\\ (1-D)\epsilon_r &= \frac{1}{E}\big[\sigma_r - \nu(\sigma_a + \sigma_r)\big]\end{aligned}\right\}\,, \tag{52}$$

which gives

$$\frac{\epsilon_r}{\epsilon_a} = \frac{\sigma_r - \nu(\sigma_r + \sigma_a)}{\sigma_a - \nu(\sigma_r + \sigma_r)} \equiv \beta\,. \tag{53}$$

The volumetric strain is then given by

$$\varepsilon_v = \epsilon_a + 2\epsilon_r = (1 + 2\beta)\epsilon_r\,. \tag{54}$$

This expression can be inserted into the chemical damage evolution law, yielding

$$\dot{D}_c = \xi\phi^s \frac{\dot{\mu}_f}{\rho_s}\big[1 - e^{-A(\varepsilon_v - \varepsilon_0)}\big]\,, \tag{55}$$

where ξ is the percentage of soluble solid in the rock. Assuming the effective stresses are fixed, the rock does not undergo mechanical damage, and so $D = D_c$ and the axial strain becomes

$$\epsilon_a = \frac{1}{(1-D_c)E}(\sigma_a - 2\nu\sigma_r)\,. \tag{56}$$

The simulation was conducted at the stress-point level utilizing the material parameters listed in Table 1. The values of the elasticity parameters E and ν were taken from MatWeb [7]. Ciantia et al. [25] observed that the dissolution of solid reduces the stiffness by dissolving the bonds between the solid grains, thereby converting the rock into granular soils. Based on their study, we assume that this bond constitutes the soluble component and represents 10% of the total volume of the solid (i.e., $\xi = 0.1$).

Using the parameters of the model, we fit the experiment data with the simulation curve as shown in Figure 3. From the initial condition up to 44 days, the axial strain is unchanged since the rock is in a stabilization state. After 44 days, CO_2 was injected and the material undergoes solid dissolution. Because of porosity increase, the stiffness of the sample degrades and the rock undergoes creep deformation. According to the trend in the slope of the curve, the axial creep deformation gradually ceases as the rock compacts and the soluble material runs out. We recall that the dissolution rate decreases with larger compression according to the exponential law. Le Guen et al. [58] did not measure the creep radial deformation, so we were unable to validate this component of the model.

Table 1. Parameters used in the simulation of creep test induced by solid dissolution on Lavoux Limestone.

Symbol	Value	Unit
E	40,000	N/mm^2
ν	0.3	–
κ_0	1.2×10^{-4}	–
a	1.0	–
b	70	–
k	10	–
A	40	–
ε_0	-1.7×10^{-2}	–
$\lvert\dot{\mu}_f\rvert$	1.4×10^{-7}	kg/mm^3/day
ρ_s	2.4×10^{-6}	kg/mm^3

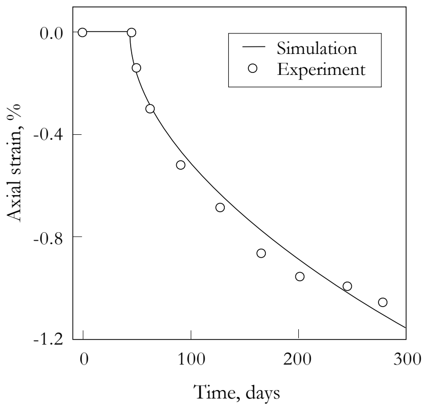

Fig. 3. Creep of limestone induced by solid dissolution. Experimental data after Le Guen et al. [58].

4.2 Three-point beam load relaxation test

The three point bending test has been commonly used as a benchmark problem in various damage models and fracture simulations [62, 78]. The problem consists of a $2000 \times 200 \times 50$ beam with a $20 \times 100 \times 50$ notch (all dimensions in mm) below the center, as shown in Figure 4. The mesh configurations are shown in Figure 5. The material properties used for the simulations are tabulated in Table 2. In this table, we assume that there is only one soluble solid and that the initial value of ϕ^s is 50%, which means that only half of the solid volume is soluble.

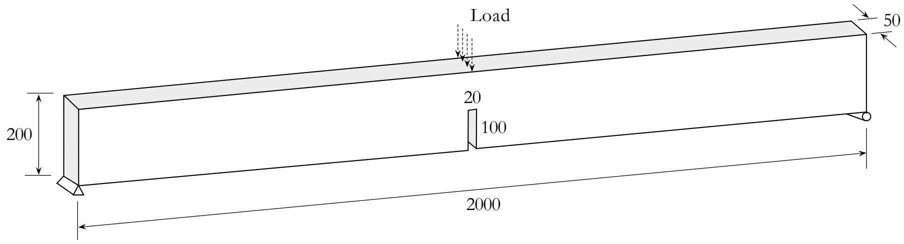

Fig. 4. Layout of the three-point beam. All dimensions in mm.

The beam is completely restrained in all directions on one end and fixed only in the vertical (i.e., in the direction of loading) and out-of plane directions on the other end. A downward displacement of 0.5 mm that increases linearly with time over a period of 0.5 days is applied at the top of the beam, after which it is held fixed. The simulations show how the damage zone continues to grow in the absence of any additional displacement due to the time-dependent damage induced by solid dissolution. The bending simulations are carried out on three different meshes with varying degrees of refinement to demonstrate the mesh insensitivity of the solution.

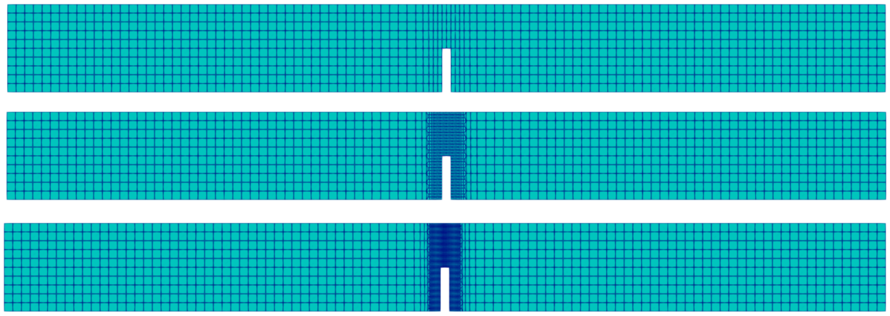

Fig. 5. Different mesh refinements: coarse, medium, and fine (from top to bottom).

Plots of the damage zone are reported in Figure 6 at $t = 0.5$ days and $t = 10$ days. The individual contributions of chemical and mechanical damage are shown separately, along with the combined total damage. Since the damage mainly occurs in the middle of the beam, we only show the result in the middle 200×200 area. From the presented results, it can be observed that the damage zone continues to propagate even after the displacement is held fixed due to the effects of chemical dissolution. The mechanical damage continues to

Table 2. Parameters used in the three-point beam load relaxation simulations.

Symbol	Value	Unit
E	30,000	N/mm^2
ν	0.2	–
κ_0	1.2×10^{-4}	–
a	1.0	–
b	385	–
k	10	–
ℓ_1	5	mm
ℓ_2	5	mm
A	200	–
ε_0	1.0×10^{-5}	–
$\lvert\dot{\mu}_f\rvert$	2×10^{-6}	kg/mm^3/day
ρ_s	2.4×10^{-6}	kg/mm^3

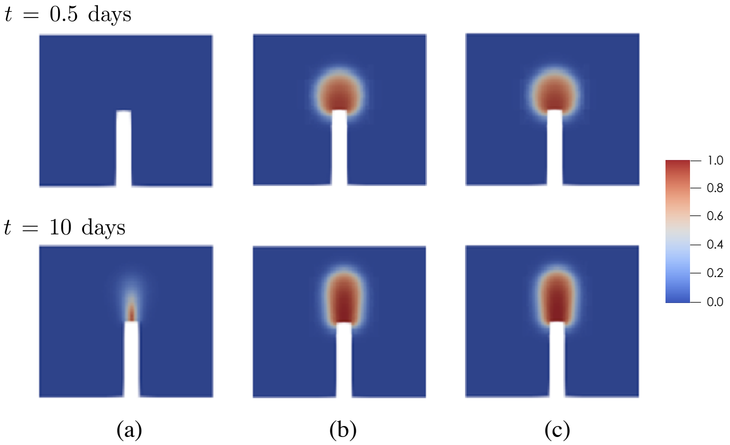

Fig. 6. Contours of damage for three-point beam load relaxation test at $t = 0.5$ days and $t = 10$ days using the medium mesh: (a) damage due to solid dissolution D_c; (b) mechanical damage D_m; and (c) total damage D. Color bar is damage variable.

increase as well, due to the nature of the coupled system. Note that dissolution damage does not develop until $t = 0.5$ days when the threshold value of the dilatational strain has been reached for the first time. Also note that mechanical damage increases as well after $t = 0.5$ days, suggesting coupling effects between mechanical and chemically induced deformations.

Figure 7 plots the time variation of the reactive force at the top of the beam where the downward displacement is applied. As shown in this figure, the slope of the curve begins to deviate from a straight line purely due to mechanical

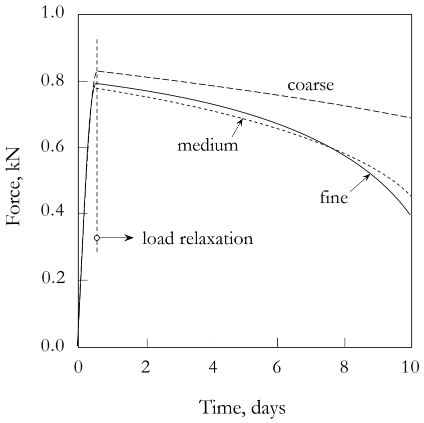

Fig. 7. Upward force reaction in the middle of the beam where the downward displacement u was prescribed versus time showing convergence of the solution as the mesh is refined.

damage up until the end of the loading phase. When the displacement is held constant, combined mechanical and chemical damage ensues. It can be observed that the damage due to dissolution reduces the reactive force almost by a half as time goes on. Furthermore, the mesh insensitivity of the solution is clearly displayed as the results of the medium and fine meshes are nearly the same. The coarse mesh follows a similar pattern, but it is too coarse to be acceptable for this particular problem. In the next section, we will conduct studies investigating the impacts of the parameters A, ε_0, ℓ_1, and ℓ_2 on the system response.

4.3 Three-point beam creep test

We conduct another set of simulations on a mesh of the same configuration (medium mesh in Figure 5) to further highlight the time-dependent damage formulation presented in this paper. As opposed to the previous section, a distributed downward line load of intensity 19.5 N/mm is applied linearly over a period of 4.5 days in place of a displacement in the middle of the beam, and is held fixed to allow the beam to creep at this load. The material parameters are given in Table 3. The initial value of ϕ^s is assumed to be 30%. Damage is shown to continue to propagate due to solid dissolution. The evolution of damage is shown in Figure 8.

We next conduct sensitivity analyses on the model parameters A, ε_0, ℓ_1, and ℓ_2 to investigate the effect of each of them on damage propagation. As expected, the parameter A depicts the rate of creep deformation, with lower values appearing to take longer time to reach the final deformed state, as shown in Figure 9a. As for the strain threshold ε_0, there is little variation in

Table 3. Parameters used in the three-point beam creep simulations.

Symbol	Value	Unit
E	30,000	N/mm^2
ν	0.2	–
κ_0	1.2×10^{-4}	–
a	1.0	–
b	70	–
k	10	–
ℓ_1	5	mm
ℓ_2	5	mm
A	500	–
ε_0	1.0×10^{-5}	–
$\lvert\dot{\mu}_f\rvert$	0.3×10^{-6}	kg/mm^3/day
ρ_s	2.4×10^{-6}	kg/mm^3

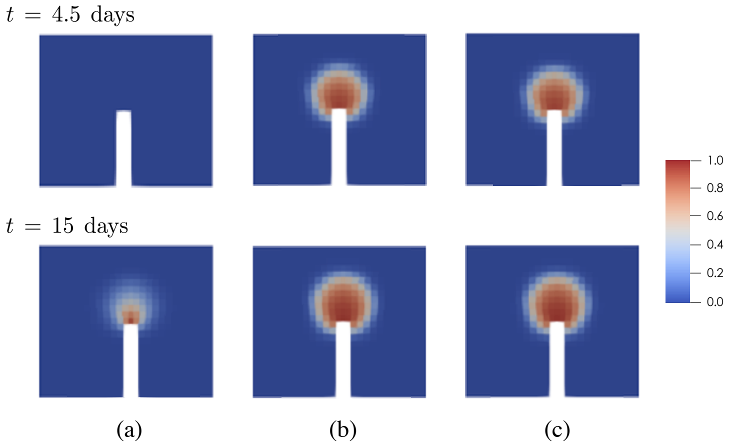

Fig. 8. Contours of damage for three-point beam creep test at $t = 4.5$ days and $t = 15$ days using the medium mesh: (a) damage due to solid dissolution D_c; (b) mechanical damage D_m; and (c) total damage D. Color bar is damage variable.

the results shown in Figure 9b. At $t = 4.5$ days, the largest threshold value plotted has already been reached ($\varepsilon_0 = 1 \times 10^{-5}$); therefore, it is expected that other smaller thresholds would have also been reached at this same time. If the threshold strain value was not reached when the loading was held fixed, the material would experience no creep-induced damage, and the curve would continue as a straight horizontal line (constant displacement). Physically, this corresponds to the dilatational strains being insufficient to allow penetration of damage-inducing fluids. The slight variation in the plots is due to the

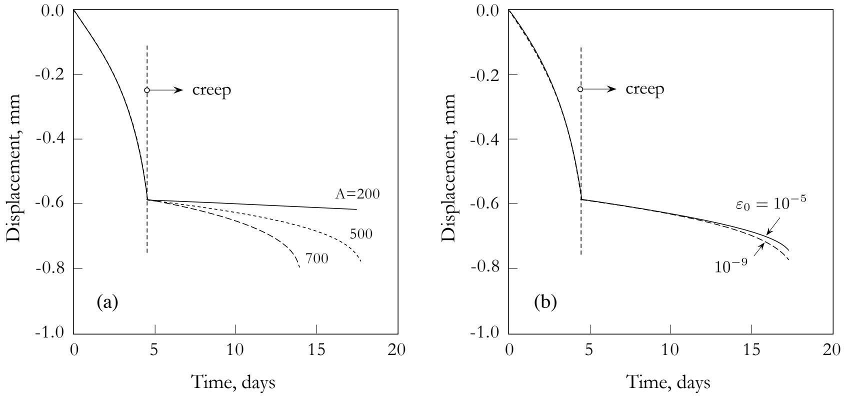

Fig. 9. Vertical displacement in the middle of the beam (where the downward vertical line load was prescribed) versus time: Influence on creep displacement of: (a) exponent coefficient A, and (b) threshold dilatational strain ε_0.

nearly insignificant effects of points near the damage zone considered to have reached the volumetric strain threshold, and thus contributing minimally to the propagation of damage.

Lastly, the effects of the variations in each of the length scales are pictured in Figure 10 showing how each affects the displacement evolution in the mechanical loading and chemical dissolution phases, respectively. The figure suggests that ℓ_1 is more influential than ℓ_2. This is because the chemical damage is harder to trigger due to the threshold ε_0, so the zone associated with chemical damage tends to be smaller. In general, appropriate length scales should be chosen to maintain stability of the solution while avoiding excessive diffusion.

Remark. It must be noted that solid dissolution could also take place on the surface of an intact solid, although this process is expected to take much longer than if the solid was highly fractured due to the smaller specific surface exposed to chemical attack. Surface erosion/dissolution is not considered in this paper, see Reference [59].

4.4 Shearing and bending of an L-beam

We again apply the model to another configuration and observe how the mechanical and chemical damage evolve in a combined shearing-bending condition. The layout and boundary conditions are shown in Figure 11. The material properties used for this simulation are tabulated in Table 4, and the initial volume fraction of the soluble solid is once again assumed to be 50%. The evolution of damage is shown in Figure 12.

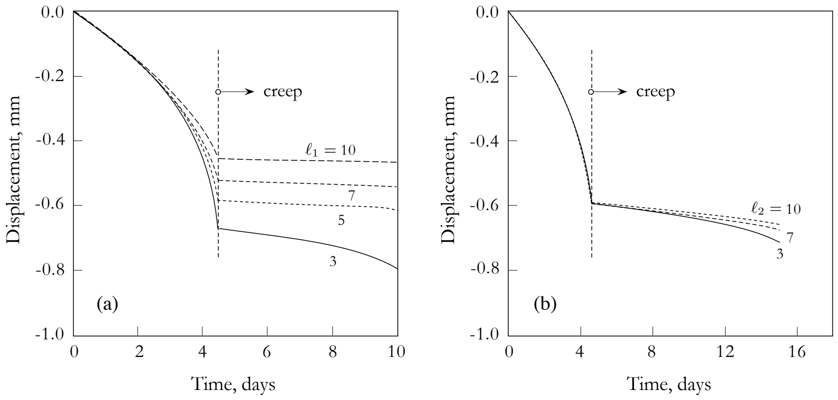

Fig. 10. Vertical displacement in the middle of the beam (where the downward vertical line load was prescribed) versus time: Influence of: (a) length scale ℓ_1 when $\ell_2 = 5$, and (b) length scale ℓ_2 when $\ell_1 = 5$. Values of ℓ in mm.

As expected, the damage zone continues to propagate well after the displacement u is held fixed. A similar phenomenon to the previous examples is observed, where even the mechanical damage continues to increase in the dissolution phase, with solid dissolution being the driving force for the damage propagation. However, in contrast to the previous example, note that the zone of localized dissolution damage is thin and suggests that a phase-field approach may have to be employed to regularize this type of damage, at least for this example. In Figure 13, we notice that the reactive force begins to decrease before $t = 0.25$ days due to mechanical damage. After around $t = 0.80$ days, the reactive force decreases drastically due to chemical damage. The result is consistent with the observations from the previous examples.

4.5 Dissolution of kaolinite around a crack tip

In this final example, we illustrate how chemical reaction induced by a pressurized fluid can influence the mechanical behavior of a fractured rock, as solid dissolution has been established to be a critical factor in the creep of soft rocks [64]. The example seeks to simulate the hydraulic fracturing process [43] as well as CO_2 sequestration [10, 21, 39, 54]. There are existing discrete [50, 53] and continuum [29, 88] models to simulate these processes, and here we show how the model proposed in this paper can be applied to model this type of problems.

The configuration of the rock volume simulated in this example is shown in Figure 14. The volume consists of a 500 × 500 × 50 block (all dimensions in mm) with an angled crack 200 mm long and 34 mm wide, and restrained in all directions at both the upper and lower left ends. The existing crack

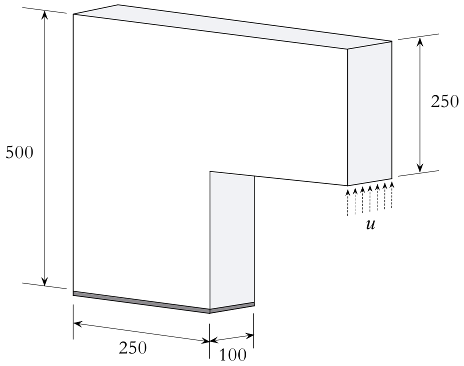

Fig. 11. Layout of the 500 × 500 L-beam. Upward displacement u is prescribed at the horizontal end. Beam is fixed at the base. All dimensions in mm.

Table 4. Parameters used in the L-beam load relaxation simulations.

Symbol	Value	Unit
E	30,000	N/mm^2
ν	0.2	–
κ_0	1.7×10^{-4}	–
a	0.98	–
b	405	–
k	10	–
ℓ_1	5	mm
ℓ_2	5	mm
A	200	–
ε_0	1.0×10^{-5}	–
$\lvert\dot{\mu}_f\rvert$	4.5×10^{-6}	kg/mm^3/day
ρ_s	2.4×10^{-6}	kg/mm^3

is representative of expected field conditions [49, 61, 100, 102]. Mechanical properties of the rock used for this simulation are similar to those of low-grade oil shale samples from the Western US [30], and are shown in Table 5. Shale is an extremely heterogeneous sedimentary rock with significant components of clay, and here we assume that the crack has intersected the clay subdomain. An erosive chemical with a known pH is injected so that the crack surface is filled with the fluid. The fluid is assumed to exert pressure perpendicular to the crack surface. The results demonstrate the mechanical behavior of the rock during injection, as well as the long-term behavior after injection.

The material parameters for the solid dissolution model is obtained as follows. Assuming the crack density-volumetric strain plot shown in Figure 1 is true for this material, we figure the value of the threshold volumetric strain

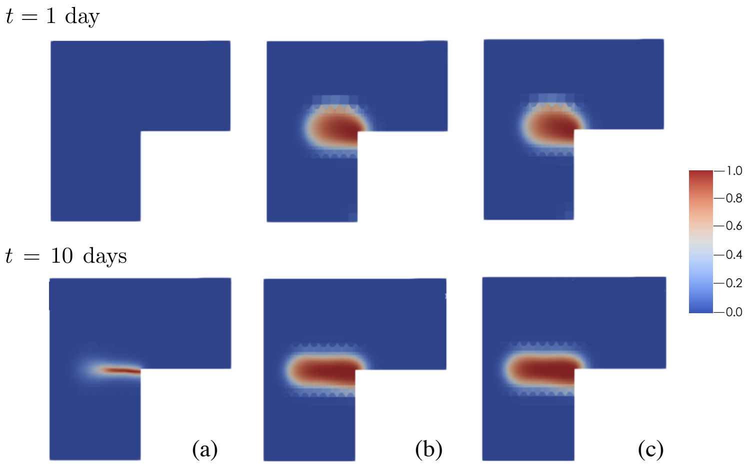

Fig. 12. Contours of damage for L-beam load relaxation test at $t = 1$ day and $t = 10$ days: (a) damage due to solid dissolution D_c; (b) mechanical damage D_m; and (c) total damage D. Color bar is damage variable.

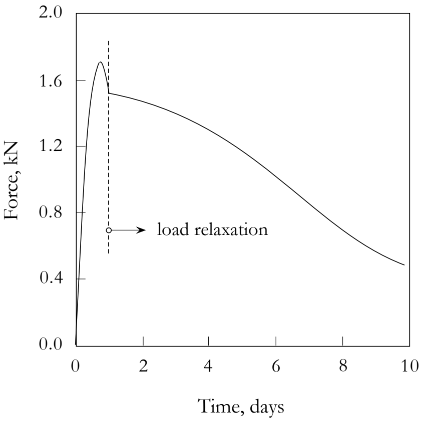

Fig. 13. Downward force reaction at the end where the prescribed displacement u was applied for the L-beam shearing-bending test.

for clay to be $\varepsilon_0 \approx -1 \times 10^{-6}$, which is slightly on the compressive side. This means that it is possible for the erosive fluid to permeate the pore spaces of the clay rock even at zero volumetric strain. Further, we figure the value of the exponential coefficient as $A \approx 40$ from the shape of the curve shown in Figure 1. Assuming the clay to be composed of kaolinite minerals, the

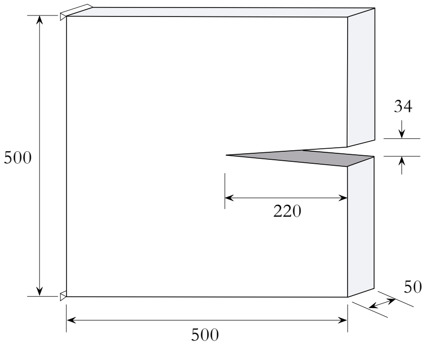

Fig. 14. Layout of the 500 × 500 rock volume with a crack filled with pressurized fluid. All dimensions in mm.

dissolution rates were measured by Cama et al. [18] and ranged as a function of temperature and fluid composition from $8 \pm 1 \times 10^{-15}$ mol/m^2/s (at 25°C and pH $= 4.5$) to $1.5 \pm 0.2 \times 10^{-11}$ mol/m^2/s (at 70°C and pH $= 0.5$). Cama et al. [18] measured these dissolution rates from input solutions at specific pH by mixing $HClO_4$ and double deionized water.

The specific kaolinite sample used in the experiment by Cama et al. [18] was the KGa-2 (Warren county, Georgia), an international reference sample of the Clay Mineral Society Source Clay Repository that was supplied by the Yale Peabody Museum. This sample was an almost pure kaolinite, containing more than 96 percent by weight of $Al_2Si_2O_5(OH)_4$. From the National Library of Medicine website (https://pubchem.ncbi.nlm.nih.gov), we find that the molecular formula $Al_2Si_2O_5(OH)_4$ is kaolin with a molar mass of 258 g/mol. The specific surface area of an acid-activated kaolinite was reported by Bhattacharyya and Gupta [11] as 16 m^2/g. Given that the intrinsic mass density of kaolinite is 2.65 g/cm^3 [42], we calculate the solid dissolution rates from dimensional analysis as follows:

$$|\dot{\mu}_f| \overset{\text{dim}}{=} \frac{\text{mol}}{\text{mm}^2 \cdot \text{s}} \times \frac{\text{g}}{\text{mol}} \times \frac{\text{mm}^2}{\text{g}} \times \frac{\text{g}}{\text{mm}^3} = \frac{\text{g}}{\text{mm}^3 \cdot \text{s}} \,.$$

Using consistent units, we obtain $|\dot{\mu}_f| \approx 8.7 \times 10^{-8}$ kg/m^3/s at 25°C and pH $= 4.5$; and $|\dot{\mu}_f| \approx 1.6 \times 10^{-4}$ kg/m^3/s at 70°C and pH $= 0.5$. We take these rates as the rates at which the kaolinite is dissolved per unit current volume of kaolinite present in the rock. Note that the dissolution rate at the higher temperature and lower pH is four orders of magnitude higher than the dissolution rate at the lower temperature and higher pH.

The increase in the width of the crack is recorded against time, as shown in Figure 15. In these simulations, we assumed that the volume fraction of kaolinite in the rock is 50%. During the injection process, the fluid is injected

Table 5. Parameters used in the kaolinite dissolution example.

Symbol	Value	Unit
E	16,000	N/mm^2
ν	0.2	–
κ_0	5×10^{-4}	–
a	1.0	–
b	300	–
k	10	–
ℓ_1	5	mm
ℓ_2	5	mm
A	40	–
ε_0	-1×10^{-6}	–
ρ_s	2.65×10^{-6}	kg/mm^3

uniformly so that the pressure on the crack surface increases linearly with time. The fluid usually generates a slow reaction from the rock [5], so the chemical dissolution during the injection process is ignored. After injection, the pressure on the crack surface is held constant and chemical dissolution begins. Figure 15 shows the calculated creep behavior due to the dissolution of kaolinite. We observe that the time scales predicted by the two dissolution processes are four orders of magnitude different reflecting the four orders of magnitude difference in dissolution rates of the mineral at the two test conditions.

The damage contour is plotted in Figure 16. We observe a similar phenomenon to the previous numerical examples in that the total damage increases due to chemical dissolution, which intensifies mechanical damage due to chemical weakening when the rock is exposed to the erosive fluid. Note that chemical damage is generally smaller than mechanical damage, so we have reduced the color bar for chemical damage for better visualization. Still, one can think of the solid dissolution near the tip of the crack as effectively leading to crack-tip blunting, which could further influence the mechanical damage evolution.

We emphasize that the gradient enhancement employed in this work is meant to regularize a diffuse damage zone in isotropic solids, and not a narrow zone of localized damage. Work is currently underway to investigate how the proposed dissolution law can be extended to anisotropic materials [46, 80, 97, 101], as well as cast the model within the framework of phase-field analysis (see [45]) to better capture the kinematics and propagation of a narrow zone of localized damage.

5 Closure

We have formulated a mathematical framework that accommodates combined chemical and mechanical damage to take place on materials such as concrete

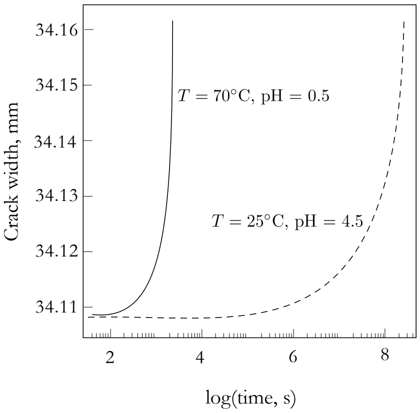

Fig. 15. Variation of crack width with time for the kaolinite dissolution example. Dissolution rates for kaolinite were derived from Cama et al. [18].

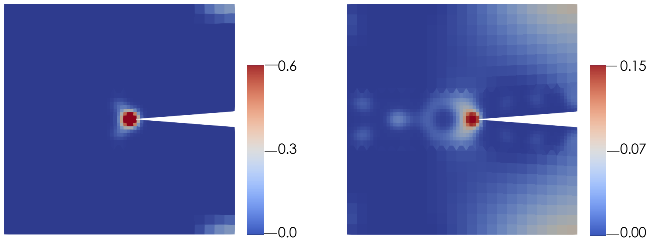

Fig. 16. Contours of mechanical damage (left) and chemical damage (right) at $t = 2 \times 10^3$ s for the kaolinite dissolution example with $T = 70°\text{C}$ and pH $= 0.5$. Note that the color bar for chemical damage has been reduced since it is smaller than the mechanical damage.

and rock that are infiltrated by an erosive fluid. Chemical damage is in the form of solid dissolution that is directly linked to the mass conservation law, which reduces the effective loading area of the material. This type of damage is then combined with mechanical damage in a multiplicative manner. Both types of damage were treated nonlocally using the gradient-enhanced formulation, leading to three-field variational equations.

Single-phase mechanical and dissolution models have been adopted for this work, leaving room for extension to multi-phase scenarios including the transport of dissolved solid by a moving fluid. However, the formulation is sufficiently general to accommodate more complicated mechanical and dissolution constitutive laws, including combined elastoplastic-damage [9] as well as mechanistically-based and experimentally validated solid dissolution laws. Apart from an ongoing work casting the model within the phase-field framework, we are also exploring the transport of dissolved solid by a moving fluid. The latter problem could have implications for similar applications in geomechanics and geotechnical engineering such as the modeling of suffusion and/or infiltration problems in soil mechanics.

CRediT authorship contribution statement

R.I. Borja conceived the project with the two co-authors, developed the combined mechanical-dissolution damage model, wrote the paper, and supervised the work. **W. Chen** developed the three-field variational formulation, created the meshes for the simulations, ran simulations, and edited the paper. **A.R. Odufisan** developed a Jacobian-free implementation of the code, figured out the material properties for the theoretical simulations, ran simulations, and edited the paper.

Acknowledgments

This work was supported by the U.S. National Science Foundation under Award Number CMMI-1914780 and the U.S. Department of Energy, Office of Science, Office of Basic Energy Sciences, Geosciences Research Program, under Award Number DE-FG02-03ER15454.

Appendix A. Linearized system

This Appendix describes how the three-field finite element equations are solved by Newton-Raphson iteration. First, we let

$$\boldsymbol{\mathcal{R}}(\boldsymbol{\mathcal{D}}) = \begin{Bmatrix} \boldsymbol{\mathcal{R}}_1 \\ \boldsymbol{\mathcal{R}}_2 \\ \boldsymbol{\mathcal{R}}_3 \end{Bmatrix} , \quad \boldsymbol{\mathcal{D}} = \begin{Bmatrix} \boldsymbol{\mathcal{D}}_1 \\ \boldsymbol{\mathcal{D}}_2 \\ \boldsymbol{\mathcal{D}}_3 \end{Bmatrix} = \begin{Bmatrix} \boldsymbol{d} \\ \boldsymbol{e} \\ \boldsymbol{l} \end{Bmatrix} . \tag{57}$$

The aim is to find the solution $\boldsymbol{\mathcal{D}}^*$ such that $\boldsymbol{\mathcal{R}}(\boldsymbol{\mathcal{D}}^*) = \boldsymbol{0}$. This requires that we evaluate the tangent operator $\boldsymbol{\mathcal{K}} = \boldsymbol{\mathcal{R}}'(\boldsymbol{\mathcal{D}})$, which has the following block structure:

$$\boldsymbol{\mathcal{K}} = \begin{bmatrix} \boldsymbol{K}_{11} & \boldsymbol{K}_{12} & \boldsymbol{K}_{13} \\ \boldsymbol{K}_{21} & \boldsymbol{K}_{22} & \boldsymbol{K}_{23} \\ \boldsymbol{K}_{31} & \boldsymbol{K}_{32} & \boldsymbol{K}_{33} \end{bmatrix} . \tag{58}$$

Before evaluating each of the submatrices of the tangent operator $\boldsymbol{\mathcal{K}}$, we first recall the following format of the algorithm: we are given the converged solution $\boldsymbol{\mathcal{D}}_n$ at time t_n and the trial values $\boldsymbol{\mathcal{D}}^{\mathrm{tr}}_{n+1} = \boldsymbol{\mathcal{D}}_n + \Delta\boldsymbol{\mathcal{D}}^k$ at the kth iteration of the Newton-Raphson loop. Thus, we can evaluate the trial value

$$\bar{\varepsilon}^{\mathrm{tr}}_{\mathrm{eq}} = \tilde{\boldsymbol{N}}\boldsymbol{e}^{\mathrm{tr}}_{n+1} \,. \tag{59}$$

This results in the discrete loading/unloading conditions

$$\kappa = \begin{cases} \bar{\varepsilon}_{\mathrm{eq}}\,, & \text{if } \bar{\varepsilon}^{\mathrm{tr}}_{\mathrm{eq}} > \kappa_n\,, \\ \kappa_n\,, & \text{otherwise}\,. \end{cases} \tag{60}$$

The derivative of the mechanical damage variable then takes either of the forms

$$D'_m(\kappa) = \begin{cases} D'_m(\bar{\varepsilon}_{\mathrm{eq}}) & \text{if } \bar{\varepsilon}^{\mathrm{tr}}_{\mathrm{eq}} > \kappa_n\,, \\ 0\,, & \text{otherwise}\,. \end{cases} \tag{61}$$

This means that D_m varies with the unknown nodal vector $\boldsymbol{e}$ only when the material is loading; otherwise, it is constant. Furthermore, differentiating (36) and (37)

$$D'_c(\bar{\lambda}) = \phi^s_n \frac{|\dot{\mu}_f|}{\rho_s}\Delta\mathrm{t}\exp\Big(-\frac{|\dot{\mu}_f|}{\rho_s}\bar{\lambda}\Delta t\Big)\,, \tag{62}$$

where $\Delta t = t - t_n$, which implies that D_c varies with the unknown nodal vector $\boldsymbol{l}$.

We now summarize the submatrices of the tangent operator $\boldsymbol{\mathcal{K}}$. For the first row block, and ignoring the $\dot{m}\boldsymbol{v}$-term for slow dissolution processes, we have

$$\boldsymbol{K}_{11} = \frac{\partial\boldsymbol{\mathcal{R}}_1}{\partial\boldsymbol{\mathcal{D}}_1} = \int_{\Omega}(1-D_c)(1-D_m)\boldsymbol{B}^{\mathsf{T}}\boldsymbol{C}^e\boldsymbol{B}\,\mathrm{d}V\,, \tag{63}$$

where $\boldsymbol{C}^e$ is the matrix form of the elasticity tensor $\mathbb{C}^e$. Furthermore, letting $\boldsymbol{b}^{\mathsf{T}} = \boldsymbol{B}^{\mathsf{T}}\hat{\boldsymbol{\sigma}}/(1-D)$, we have

$$\boldsymbol{K}_{12} = \frac{\partial\boldsymbol{\mathcal{R}}_1}{\partial\boldsymbol{\mathcal{D}}_2} = -\int_{\Omega}(1-D_c)D'_m(\kappa)\boldsymbol{b}^{\mathsf{T}}\tilde{\boldsymbol{N}}\,\mathrm{d}V \tag{64}$$

and

$$\boldsymbol{K}_{13} = \frac{\partial\boldsymbol{\mathcal{R}}_1}{\partial\boldsymbol{\mathcal{D}}_3} = -\int_{\Omega}(1-D_m)D'_c(\bar{\lambda})\boldsymbol{b}^{\mathsf{T}}\tilde{\boldsymbol{N}}\,\mathrm{d}V\,. \tag{65}$$

For the second row block, we note that the local equivalent strain $\varepsilon_{\mathrm{eq}}$ varies with the full strain tensor $\boldsymbol{\epsilon}$ so that one can obtain the 6×1 column vector

$$\boldsymbol{\delta} = \frac{\partial\varepsilon_{\mathrm{eq}}}{\partial\hat{\boldsymbol{\epsilon}}}\,, \tag{66}$$

where $\hat{\boldsymbol{\epsilon}}$ is the full strain tensor in Voigt form. Thus, we get

$$\boldsymbol{K}_{21} = \frac{\partial\boldsymbol{\mathcal{R}}_2}{\partial\boldsymbol{\mathcal{D}}_1} = -\int_{\Omega}\tilde{\boldsymbol{N}}^{\mathsf{T}}\boldsymbol{\delta}^{\mathsf{T}}\boldsymbol{B}\,\mathrm{d}V\,. \tag{67}$$

Furthermore,

$$\boldsymbol{K}_{22} = \int_{\Omega} \tilde{\boldsymbol{N}}^{\mathsf{T}} \tilde{\boldsymbol{N}} \, \mathrm{d}V + \int_{\Omega} \boldsymbol{E}^{\mathsf{T}} \ell_1^2 \, \boldsymbol{E} \, \mathrm{d}V \tag{68}$$

and $\boldsymbol{K}_{23} = \mathbf{0}$.

For the third row block, we note that the local value of λ varies with the full strain tensor $\boldsymbol{\epsilon}$ through the volumetric component ε_v so that one can obtain the 6×1 column vector

$$\boldsymbol{\theta} = \lambda'(\varepsilon_v)\mathbf{1} \, , \tag{69}$$

where $\mathbf{1}$ is the Kronecker delta tensor in Voigt form. Thus,

$$\boldsymbol{K}_{31} = \frac{\partial \boldsymbol{\mathcal{R}}_3}{\partial \boldsymbol{\mathcal{D}}_1} = - \int_{\Omega} \tilde{\boldsymbol{N}}^{\mathsf{T}} \boldsymbol{\theta}^{\mathsf{T}} \boldsymbol{B} \, \mathrm{d}V \, . \tag{70}$$

Lastly, $\boldsymbol{K}_{32} = \mathbf{0}$ and

$$\boldsymbol{K}_{33} = \int_{\Omega} \tilde{\boldsymbol{N}}^{\mathsf{T}} \tilde{\boldsymbol{N}} \, \mathrm{d}V + \int_{\Omega} \boldsymbol{E}^{\mathsf{T}} \ell_2^2 \, \boldsymbol{E} \, \mathrm{d}V \, . \tag{71}$$

The tangent operator $\boldsymbol{\mathcal{K}}$ is not symmetric.

References

[1] Akono AT, Druhan JL, Dávila G, Tsotsis T, Jessen K, Fuchs S, Crandall D, Shi Z, Dalton L, Tkach MK, Goodman AL, Frailey S, Werth CJ (2019). A review of geochemical-mechanical impacts in geological carbon storage reservoirs. Greenhouse Gases: Science and Technology, 9(3):474–504.

[2] Anderson RY, Kirkland DW (1980). Dissolution of salt deposits by brine density flow. Geology 8(2):66–69.

[3] Ao X, Lu Y, Tang J, Chen Y, Li H (2017). Investigation on the physics structure and chemical properties of the shale treated by supercritical CO_2. Journal of CO_2 Utilization, 20:274–281.

[4] Ausloos M, Salmon E, Vandewalle N (1999). Water invasion, freezing, and thawing in cementitious materials. Cement and Concrete Research 29:209–213.

[5] Baines SJ, Worden RH (2004). The long-term fate of CO_2 in the subsurface: Natural analogues for CO_2 storage. Geological Society, London, Special Publications, 233(1):59–85.

[6] Bagni FL, Bezerra FH, Balsamo F, Maia RP, Dall'Aglio M (2020). Karst dissolution along fracture corridors in an anticline hinge, Jandaíra Formation, Brazil: Implications for reservoir quality. Marine and Petroleum Geology 115:104249.

[7] Bauccio M (1989). ASM Engineered Materials Reference Book. ASM International (OH).

[8] Bennett KC, Berla LA, Nix WD, Borja RI (2015) Instrumented nanoindentation and 3D mechanistic modeling of a shale at multiple scales. Acta Geotechnica 10:1–14.

[9] Bennett, K.C., Borja, R.I. (2018). Hyper-elastoplastic/damage modeling of rock with application to porous limestone. International Journal of Solids and Structures 143:218–231.

[10] Benson SM, Cole DR (2008). CO_2 sequestration in deep sedimentary formations. Elements, 4(5):325–331.

[11] Bhattacharyya KG, Gupta SS (2009). Adsorptive accumulation of Cd(II), Co(II), Cu(II), Pb(II), and Ni(II) from water onto kaolinite: Influence of acid activation. Adsorption Science & Technology 27(1):47–68.

[12] Black JR, Carroll SA, Haese RR (2015). Rates of mineral dissolution under CO_2 storage conditions. Chemical Geology 399:134–144.

[13] Borja RI, Yin Q, Zhao Y (2020). Cam-Clay plasticity. Part IX: On the anisotropy, heterogeneity, and viscoplasticity of shale. Computer Methods in Applied Mechanics and Engineering 360:112695.

[14] Borja RI (2013). Plasticity Modeling and Computation, Springer-Verlag, Berlin-Heidelberg.

[15] Borja RI (2020). Computational Poromechanics, Lecture Notes, Stanford University.

[16] Borja RI, Choo J (2016). Cam-Clay plasticity, Part VIII: A constitutive framework for porous materials with evolving internal structure. Computer Methods in Applied Mechanics and Engineering 309:653–679.

[17] Borja RI (2006). On the mechanical energy and effective stress in saturated and unsaturated porous continua. International Journal of Solids and Structures 43(6):1764–1786.

[18] Cama J, Metz V, Ganor J (2002). The effect of pH and temperature on kaolinite dissolution rate under acidic conditions. Geochimica et Cosmochimica Acta 66(22):3913–3926.

[19] Camargo JT, White JA, Borja RI (2021) A macroelement stabilization for mixed finite element/finite volume discretizations of multiphase poromechanics. Computational Geosciences 25:775–792.

[20] Camargo JT, White JA, Castelleto N, Borja RI (2021) Preconditioners for multiphase poromechanics with strong capillarity. International Journal for Numerical and Analytical Methods in Geomechanics 45(9):1141–1168.

[21] Chen M, Hosking LJ, Sandford RJ, Thomas HR (2020). A coupled compressible flow and geomechanics model for dynamic fracture aperture during carbon sequestration in coal. International Journal for Numerical and Analytical Methods in Geomechanics 44(13):1727–49.

[22] Choo J, Borja RI (2015). Stabilized mixed finite elements for deformable porous media with double porosity. Computer Methods in Applied Mechanics and Engineering 293:131–154.

[23] Choo J, White JA, Borja RI (2016). Hydromechanical modeling of unsaturated flow in double porosity media. International Journal of Geomechanics, DOI: 10.1061/(ASCE)GM.1943-5622.0000558, D4016002.

[24] Choo J, Semnani SJ, White JA (2021). An anisotropic viscoplasticity model for shale based on layered microstructure homogenization. International Journal for Numerical and Analytical Methods in Geomechanics 45(4):502–520.

[25] Ciantia MO, Castellanza R, Di Prisco C (2015). Experimental study on the water-induced weakening of calcarenites. Rock Mechanics and Rock Engineering 48(2):441–461.

[26] De Vree JHP, Brekelmans WAM, van Gils, MAJ (1995). Comparison of nonlocal approaches in continuum damage mechanics. Computers & Structures 55(4):581–588.

[27] del Castillo EM, Fávero Neto AH, Borja RI (2021) Fault propagation and surface rupture in geologic materials with a meshfree continuum method. Acta Geotechnica 16:2463–2486.

[28] del Castillo EM, Fávero Neto AH, Borja RI (2021) A continuum meshfree method for sandbox-style numerical modeling of accretionary and doubly vergent wedges. Journal of Structural Geology 153:104466.

[29] Duddu R, Jiménez S, Bassis J (2020). A non-local continuum porodamage mechanics model for hydrofracturing of surface crevasses in grounded glaciers. Journal of Glaciology 66(257):415–29.

[30] Eseme E, Urai J, Krooss B, Littke R (2007). Review of mechanical properties of oil shales: Implications for exploitation and basin modelling. Oil Shale, 24(2):159–174.

[31] Espinoza DN, Santamarina JC (2012). Clay interaction with liquid and CO_2: The relevance of electrical and capillary forces. International Journal of Greenhouse Gas Control, 10, 351–362.

[32] Fávero Neto AH, Askarinejad A, Springman SM, Borja RI (2020). Simulation of debris flow on an instrumented test slope using an updated Lagrangian continuum particle method. Acta Geotechnica 15:2757–2777.

[33] Fávero Neto AH, Borja RI (2018). Continuum hydrodynamics of dry granular flows employing multiplicative elastoplasticity. Acta Geotechnica 13:1027–1040.

[34] Feng G, Kang Y, Sun ZD, Wang XC, Hu YQ (2019). Effects of supercritical CO_2 adsorption on the mechanical characteristics and failure mechanisms of shale. Energy, 173:870–882.

[35] Fein JB, Walther JV (1987). Calcite solubility in supercritical CO_2-H_2O fluids. Geochimica et Cosmochimica Acta 51:1665–1673.

[36] Grgic D (2011). Influence of CO_2 on the long-term chemomechanical behavior of an oolitic limestone. Journal of Geophysical Research: Solid Earth, 116(B7).

[37] Gong CG, Wang W, Shao JF, Wang RB, Feng XW (2021). Effect of water chemical corrosion on mechanical properties and failure modes

of pre-fissured sandstone under uniaxial compression. Acta Geotechnica 16(4):1083–99.

[38] Guo Y, Deng P, Yang C, Chang X, Wang L, Zhou J (2018). Experimental investigation on hydraulic fracture propagation of carbonate rocks under different fracturing fluids. Energies 11:3502.

[39] Ha SJ, Kim Y, Yun TS (2021). Development of microcracks in granitic rock by liquid CO2 fracturing. International Journal of Rock Mechanics and Mining Sciences 146:104876.

[40] Hangx S, van der Linden A, Marcelis F, Bauer A (2013). The effect of CO_2 on the mechanical properties of the Captain Sandstone: Geological storage of CO_2 at the Goldeneye field (UK). International Journal of Greenhouse Gas Control, 19, 609–619.

[41] Herz-Thyhsen RJ, Kaszuba JP, Dewey JC (2019). Dissolution of minerals and precipitation of an aluminosilicate phase during experimentally simulated hydraulic fracturing of a mudstone and a tight sandstone in the Powder River Basin, WY. Energy & Fuels 33:3947–3956.

[42] Holtz DR, Kovacs DW (1981) An Introduction to Geotechnical Engineering. Prentice-Hall, Inc.

[43] Hou MZ, Li M, Gou Y, Feng W (2021). Numerical simulation and evaluation of the fracturing and tight gas production with a new dimensionless fracture conductivity (FCD) model. Acta Geotechnica 16(4):985–1000.

[44] Hueckel T, Hu L (2004). Chemo-mechanical coupling and damage enhanced dissolution at intergranular contact. In: Proceedings of the Ninth Symposium on Numerical Models in Geomechanics, Balkema, Rotterdam, pp. 349–353.

[45] Ip SCY, Borja RI (2022). A phase-field approach for compaction band formation due to grain crushing. International Journal for Numerical and Analytical Methods in Geomechanics 46(16):2965–2987.

[46] Jin W, Arson C (2018). Anisotropic nonlocal damage model for materials with intrinsic transverse isotropy. International Journal of Solids and Structures 139–140:29–42.

[47] Ju JW (1990). Isotropic and anisotropic damage variables in continuum damage mechanics. Journal of Engineering Mechanics 116(12):2764–2770.

[48] Kang Q, Zhang D, Chen S (2003). Simulation of dissolution and precipitation in porous media. Journal of Geophysical Research: Solid Earth 108(B10):2505, doi:10.1029/2003JB002504.

[49] Kang G, Ning Y, Chen P, Pang S, Shao Y (2021). Comprehensive simulations of rock fracturing with pre-existing cracks by the numerical manifold method. Acta Geotechnica 14:1–20.

[50] Krzaczek M, Nitka M, Kozicki J, Tejchman J (2020). Simulations of hydro-fracking in rock mass at meso-scale using fully coupled DEM/CFD approach. Acta Geotechnica 15(2):297–324.

[51] Kuhl E, Ramm E, de Borst R (2000) An anisotropic gradient damage model for quasi-brittle materials. Computer Methods in Applied Mechanics and Engineering 183:87–103.

[52] Kuhl D, Bangert F, Meschke G (2004) Coupled chemo-mechanical deterioration of cementitious materials Part II: Numerical methods and simulations. International Journal of Solids and Structures 41(1):41–67.

[53] Kwok CY, Duan K, Pierce M (2020). Modeling hydraulic fracturing in jointed shale formation with the use of fully coupled discrete element method. Acta Geotechnica 15(1):245–64.

[54] Lackner KS (2003). A guide to CO_2 sequestration. Science 300(5626):1677–1678.

[55] Lasaga AC (1984). Chemical kinetics of water-rock interactions. Journal of Geophysical Research: Solid Earth 89(B6):4009–4025.

[56] Lasaga AC (2014). Kinetic Theory in the Earth Sciences. Princeton University Press.

[57] Le Bellégo, C., Pijaudier-Cabot, G., Gérard, B., Dubé, J.-F., Molez, L. (2003). Coupled mechanical and chemical damage in calcium leached cementitious structures. Journal of Engineering Mechanics 129(3):333–341.

[58] Le Guen Y, Renard F, Hellmann R, Brosse E, Collombet M, Tisserand D, Gratier JP (2007). Enhanced deformation of limestone and sandstone in the presence of high fluids. Journal of Geophysical Research: Solid Earth, 112(B5).

[59] Li L, Rivas E, Gracie R, Dusseault MB (2021). Methodology for the nonlinear coupled multi-physics simulation of mineral dissolution. International Journal for Numerical and Analytical Methods in Geomechanics, 45(15):2193–2213.

[60] Li J, Xie F, Zhao G, Li L (2020). Experimental and numerical investigation of cast-in-situ concrete under external sulfate attack and drying-wetting cycles. Construction and Building Materials 249:118789.

[61] Liao J, Gou Y, Feng W, Mehmood F, Xie Y, Hou Z (2020). Development of a full 3D numerical model to investigate the hydraulic fracture propagation under the impact of orthogonal natural fractures. Acta Geotechnica 15(2):279–95.

[62] Linder C, Zhang X (2013). A marching cubes based failure surface propagation concept for three-dimensional finite elements with non-planar embedded strong discontinuities of higher-order kinematics. International Journal for Numerical Methods in Engineering 96(6):339–372.

[63] Liu E, Lai Y (2020). Thermo-poromechanics-based viscoplastic damage constitutive model for saturated frozen soil. International Journal of Plasticity 128:102683.

[64] Liu Z, Zhou C, Li, B, Zhang L, Liang Y (2020). Effects of grain dissolution–diffusion sliding and hydro-mechanical interaction on the creep deformation of soft rocks. Acta Geotechnica 15(5):1219–1229.

[65] Lu Y, Chen X, Tang J, Li H, Zhou L, Han S, Ge Z, Xia B, Shen H, Zhang J (2019). Relationship between pore structure and mechanical properties of shale on supercritical carbon dioxide saturation. Energy, 172, 270–285.

[66] Lyu Q, Long X, Ranjith PG, Tan J, Kang Y, Wang Z (2018). Experimental investigation on the mechanical properties of a low-clay shale with different adsorption times in sub-/super-critical CO_2. Energy, 147:1288–1298.

[67] Madland MV, Finsnes A, Alkafadgi A, Risnes R, Austad T (2006). The influence of CO_2 gas and carbonate water on the mechanical stability of chalk. Journal of Petroleum Science and Engineering 51:149–168.

[68] Mazars J, Pijaudier-Cabot G (1989). Continuum damage theory—Application to concrete. Journal of Engineering Mechanics 115:345–365

[69] Odumabo SM, Karpyn ZT, Ayala LFH Ayala (2014). Investigation of gas flow hindrance due to fracturing fluid leakoff in low permeability sandstones. Journal of Natural Gas Science and Engineering 17:1–12.

[70] Otsuka K, Date H (2000). Fracture process zone in concrete tension specimen. Engineering Fracture Mechanics 65(2–3):111–131.

[71] Pechukas P (1981). Transition state theory. Annual Review of Physical Chemistry, 32(1):159–177.

[72] Peerlings RHJ, de Borst R, Brekelmans, WAM, Geers MGD (1998). Gradient-enhanced damage modelling of concrete fracture. Mechanics of Cohesive-Frictional Materials 3:323–342.

[73] Peerlings RHJ, de Borst R, Brekelmans WAM, De Vree JHP (1996). Gradient enhanced damage for quasi-brittle materials. International Journal for Numerical Methods in Engineering 39(19):3391–3403.

[74] Pigazzini MS, Kamensky D, van Iersel DAP, Alaydin MD, Remmers JJC, Bazilevs Y (2019). Gradient-enhanced damage modeling in Kirchhoff–Love shells: Application to isogeometric analysis of composite laminatess. Computer Methods in Applied Mechanics and Engineering 346:152–179

[75] Pijaudier-Cabot G, Bažant Z (1987). Nonlocal damage theory. Journal of Engineering Mechanics 113(10):1512–1533.

[76] Qin S, Zou D, Liu T, Jivkov A (2020). A chemo-transport-damage model for concrete under external sulfate attack. Cement and Concrete Research 132:106048.

[77] Razanica S, Larsson R, Josefson BL (2019). A ductile fracture model based on continuum thermodynamics and damage. Mechanics of Materials 139:103197.

[78] Rots JG, Nauta P, Kuster GMA, Blaauwendraad J (1985). Smeared crack approach and fracture localization in concrete. HERON 30(1), Delft University of Technology, The Netherlands.

[79] Sarkar S, Singh IV, Mishra BK (2020). A Thermo-mechanical gradient enhanced damage method for fracture. Computational Mechanics 66:1399–1426.

[80] Semnani SJ, White JA, Borja RI (2016). Thermoplasticity and strain localization in transversely isotropic materials based on anisotropic critical state plasticity. International Journal for Numerical and Analytical Methods in Geomechanics 40(18):2423–2449.

[81] Shen X, Ding J, Arson C, Chester JS, Chester FM (2021). Micromechanical modeling for rate-dependent behavior of salt rock under cyclic loading. International Journal for Numerical and Analytical Methods in Geomechanics 45(1):28–44.

[82] Simo JC, Ju JW (1987). Strain- and stress-based continuum damage models—I. Formulation. International Journal of Solids and Structures 23(7):821–840.

[83] Spyropoulos C, Griffith WJ, Scholz CH, Shaw BE (1999). Experimental evidence for different strain regimes of crack populations in a clay model. Geophysical Research Letters. 26(8):1081–1084.

[84] Truhlar DG, Garrett BC, Klippenstein SJ (1996). Current status of transition-state theory. Journal of Physical Chemistry 100(31):12771–12800.

[85] Vanorio T, Nur A, Ebert Y (2011). Rock physics analysis and time-lapse rock imaging of geochemical effects due to the injection of CO_2 into reservoir rocks. Geophysics, 76(5), O23–O33.

[86] Vialle S, Vanorio T (2011). Laboratory measurements of elastic properties of carbonate rocks during injection of reactive CO_2-saturated water. Geophysical Research Letters, 38(1), doi:10.1029/2010GL045606.

[87] Voyiadjis, G.Z., Taqieddin, Z.N., Kattan, P.I. (2008). Anisotropic damage-plasticity model for concrete. International Journal of Plasticity 24(10):1946–1965.

[88] Wang D, Zlotnik S, Díez P (2020). A numerical study on hydraulic fracturing problems via the proper generalized decomposition method. CMES: computer modeling in engineering and sciences 122(2):703–20.

[89] White JA, Borja RI (2008). Stabilized low-order finite elements for coupled solid-deformation/fluid-diffusion and their application to fault zone transients. Computer Methods in Applied Mechanics and Engineering 197:4353–4366.

[90] Wu F, Chen J, Zou Q (2019). A nonlinear creep damage model for salt rock. International Journal of Damage Mechanics 28(5):758–771.

[91] Yao, Mingbo and Li, Jingpei (2019). Effect of the degradation of concrete friction piles exposed to external sulfate attack on the pile bearing capacity. Ocean Engineering 173:599–607.

[92] Yin H, Zhou J, Xian X, Jiang Y, Lu Z, Tan J, Liu G. (2017). Experimental study of the effects of sub-and super-critical CO_2 saturation on the mechanical characteristics of organic-rich shales. Energy, 132:84–95.

[93] Yin Q, Liu Y, Borja RI (2021). Mechanisms of creep in shale from nanoscale to specimen scale. Computers and Geotechnics 136:104138.

[94] Zhang S, Xian X, Zhou J, Zhang L (2017). Mechanical behaviour of Longmaxi black shale saturated with different fluids: an experimental study. RSC Advances, 7(68):42946–42955.

[95] Zhang Q, Choo J, Borja RI (2019). On the preferential flow patterns induced by transverse isotropy and non-Darcy flow in double porosity media. Computer Methods in Applied Mechanics and Engineering 353:570–592.

[96] Zhang Q, Borja RI (2021). Poroelastic coefficients for single and double porosity media. Acta Geotechnica, https://doi.org/10.1007/s11440-021-01184-y.

[97] Zhao Y, Semnani SJ, Yin Q, Borja RI (2018). On the strength of transversely isotropic rocks. International Journal for Numerical and Analytical Methods in Geomechanics 42(16):1917–1934.

[98] Zhao Y, Borja RI (2020). A continuum framework for coupled solid deformation-fluid flow through anisotropic elastoplastic porous media. Computer Methods in Applied Mechanics and Engineering, 369, 113225.

[99] Zhao Y, Borja RI (2021). Anisotropic elastoplastic response of double-porosity media. Computer Methods in Applied Mechanics and Engineering, 380, 113797.

[100] Zhao Y, Gao Y, Wu S, Chen L, Zhang C (2021). Experimental and numerical study of failure characteristics of brittle rocks with single internal 3D open-type flaw. Acta Geotechnica. 2:1–27.

[101] Zhao Y, Borja RI (2022). A double-yield-surface plasticity theory for transversely isotropic rocks. Acta Geotechnica, DOI:10.1007/s11440-022-01605-6.

[102] Zhu Q, Li D, Han Z, Xiao P, Li B (2021). Failure characteristics of brittle rock containing two rectangular holes under uniaxial compression and coupled static-dynamic loads. Acta Geotechnica 7:1–22.

[103] Zou Y, Li S, Ma X, Zhang S, Li N, Chen M (2018). Effects of CO_2-brine-rock interaction on porosity/permeability and mechanical properties during supercritical-CO_2 fracturing in shale reservoirs. Journal of Natural Gas Science and Engineering, 49, 157–168.